# A Machine Learning Force Field for Lithium Sulfide-Based Glassy Electrolytes and its Comprehensive Validation and Application

**Authors**: Rui Zhou, Kun Luo, Steve W. Martin, and Qi An\*

Department of Materials Science and Engineering, Iowa State University, Ames, Iowa 50011, United States

\*Corresponding Author's email: qan@iastate.edu

#### **Abstract**:

Sulfide-based solid electrolytes (SEs) are emerging as compelling materials for all-solid-state batteries (ASSBs), primarily due to their high ionic conductivities and robust mechanical stability. In particular, glassy SEs (GSEs) comprising mixed Si and P glassformers show promise, thanks to their efficient synthesis process and their intrinsic ability to prevent lithium dendrite growth. However, to date the complexity of their glassy structures hinders a complete understanding of the relationships between their structures and properties. Here, new machine learning force field (ML-FF) specifically designed for lithium sulfide-based GSEs has been developed. This ML-FF has been used to investigate the structural characteristics, mechanical properties, and lithium ionic conductivities in binary lithium thiosilicate and lithium thiophosphate GSEs, as well as their ternary mixed glassformer (MGF) lithium thiosilicophosphate GSEs. Molecular dynamic (MD) simulations using the ML-FF were conducted to explore the glass structures in varying compositions, including binary Li<sub>2</sub>S-SiS<sub>2</sub> and Li<sub>2</sub>S-P<sub>2</sub>S<sub>5</sub>, as well as ternary Li<sub>2</sub>S-SiS<sub>2</sub>-P<sub>2</sub>S<sub>5</sub>. The simulations with the ML-FF yielded consistent results in terms of density, elastic modulus, radial distribution functions, and neutron structure factors, compared to DFT and experimental work. A key focus of this study was to investigate the local environments of Si and P molecular clusters. We discovered that most Si atoms in the Li<sub>2</sub>S-SiS<sub>2</sub> GSE are situated in an edge-sharing environment, while the Li<sub>2</sub>S-P<sub>2</sub>S<sub>5</sub> glass contained a minor proportion of edge-sharing P<sub>2</sub>S<sub>6</sub><sup>2</sup>environments. In the ternary 60Li<sub>2</sub>S-32SiS<sub>2</sub>-8P<sub>2</sub>S<sub>5</sub> glass, the ML-FF predicted similar P environments as observed in the binary Li<sub>2</sub>S-P<sub>2</sub>S<sub>5</sub> glass. Additionally, it indicated the coexistence of corner and edge-sharing between PS<sub>4</sub> and SiS<sub>4</sub> tetrahedra in this ternary composition. Concerning lithium ionic conductivity at 300K, all studied glass compositions exhibited similar magnitudes and followed the Arrhenius relationship. The 50Li<sub>2</sub>S-50SiS<sub>2</sub> glass displayed the lowest conductivity at 2.1 mS/cm, while the 75Li<sub>2</sub>S-25P<sub>2</sub>S<sub>5</sub> composition exhibited the highest at 3.6

mS/cm. The ternary glass showed a conductivity of 2.57 mS/cm, sitting between the two. Interestingly, the predicted conductivities were about an order of magnitude higher than experimental values for the binary glasses but aligning more closely with that of the ternary glass. Moreover, an in-depth analysis of lithium-ion diffusion over the MD trajectory in the ternary glass demonstrated a significant correlation between diffusion pathways and the rotational dynamics of nearby SiS<sub>4</sub> or PS<sub>4</sub> tetrahedra. The ML-FF developed in this study shows immense potential as a versatile tool for exploring a broad spectrum of solid-state and mixed-former sulfide-based electrolytes.

#### 1. Introduction

All-solid-state lithium-ion batteries stand as a revolutionary advancement in energy storage technology, offering unprecedented safety benchmarks and energy density metrics [1]. Among the various candidates, sulfide-based solid state electrolytes (SSEs) are particularly promising [2]. These electrolytes generally fall into three categories: crystalline, glass-ceramic, and glass. The glass type, in particular, garners considerable attention due to its lack of grain boundaries, unlike its crystalline counterparts [3,4]. This unique characteristic is crucial for inhibiting lithium dendrite growth, thereby enhancing battery safety and improving mechanical and thermal properties [5,6]. Two main glass solid electrolyte (GSE) systems have dominated research over the years: lithium thiophosphate (Li<sub>2</sub>S+P<sub>2</sub>S<sub>5</sub>, LPS) [7–9] and the lithium thiosilicate (Li<sub>2</sub>S+SiS<sub>2</sub>, LiSiS) [10–12]. However, their practical applications are hindered by synthesis challenges and limited compatibility with Li metal anodes.

In terms of compatibility, Kennedy *et al.* [13] have pointed out that in SiS<sub>2</sub>-based GSEs, SiS<sub>2</sub> and Li react to form Si and Li<sub>2</sub>S. Further reactions between Si and Li can produce Li-Si alloys, potentially degrading the performance of SiS<sub>2</sub>-based GSEs. Regarding synthesis challenges, the high vapor pressure of P<sub>2</sub>S<sub>5</sub> [13,14] makes the LPS glass more suitable for synthesis through ball milling rather than the melt-quench method. Introducing a second glass former can mitigate vaporization issues and improve glass-forming ability. For instance, adding another glass former has been shown to enhance the Li metal stability of SiS<sub>2</sub>-based glasses [13,14]. Kennedy *et al.* synthesized 60Li<sub>2</sub>S-40[xSiS<sub>2</sub>-(100-x)P<sub>2</sub>S<sub>5</sub>] GSEs and found that the composition 60Li<sub>2</sub>S-32SiS<sub>2</sub>-8P<sub>2</sub>S<sub>5</sub> exhibits the highest conductivity of 0.7 mS/cm at 25°C [13]. Additionally, Zhao *et al.* synthesized various glass compositions, including 60Li<sub>2</sub>S-32SiS<sub>2</sub>-8P<sub>2</sub>S<sub>5</sub>, an oxy-sulfide GSE of 67Li<sub>2</sub>S-33(80SiS<sub>2</sub>-20P<sub>2</sub>O<sub>5</sub>), and a LiPON-doped oxy-sulfide GSE [14]. Their studies revealed that the incorporation of oxygen and nitrogen into the GSE lowers its conductivity but raises the critical current density (CCD) to 1.76 mA/cm<sup>2</sup>, these authors attributed this increased stability to the formation of protective bridging oxygen (BO) atoms at the Si sites [14].

SSEs have experienced significant advancements in design and understanding, thanks, in part, to the use of computational modeling and simulations. Techniques like density functional theory (DFT), reverse Monte Carlo (RMC), molecular dynamics (MD) with classical force fields, and ab-

initio molecular dynamics (AIMD) simulations are instrumental in unraveling the atomistic mechanisms underlying structural properties and diffusion processes in SSEs, deepening our knowledge of their intrinsic properties [3]. RMC, a cost-effective computational method, has been utilized to model Li<sub>2</sub>S-SiS<sub>2</sub> and Li<sub>2</sub>S-P<sub>2</sub>S<sub>5</sub> glass structures [11,15], effectively mimicking experimental structures. However, RMC methods do not provide insights into dynamic properties such as ionic conductivity. MD techniques, on the other hand, have been applied to explore the dynamic properties of SSEs. Baba et al. used melt-quench in their MD studies to model LPS GSEs, estimating their ionic conductivities to be around 10<sup>-5</sup> S/cm at 25 °C. Ohkubo et al. employed artificial intelligence MD (AIMD) to investigate the Li-ion conduction mechanism in 70Li<sub>2</sub>S-30P<sub>2</sub>S<sub>5</sub> glass and Li<sub>7</sub>P<sub>3</sub>S<sub>11</sub> crystal [16], noting tetrahedra rotationassisted Li<sup>+</sup> ion migration ocurred only in the glass phase. Sadowski et al. systematically examined the stability and conductivity of LPS glass, including the effects of various quench parameters on its properties [17]. However, the high cost and computational intensity of DFT and AIMD simulations limit their application to small systems and short time scales, potentially constraining the study of ergodic yet non-equilibrium structures in glassy phases and dynamics [18].

To overcome these limitations, Ariga *et al.* developed a classical force field of COMPASS Class II forms for both amorphous and crystalline of Li<sub>2</sub>S-P<sub>2</sub>S<sub>5</sub> [19], exploring their structures and conductivity properties. They predicted a highest conductivity of 5.3 × 10<sup>-2</sup> S/cm in Li<sub>7</sub>P<sub>3</sub>S<sub>11</sub> crystals, while 67Li<sub>2</sub>S-33P<sub>2</sub>S<sub>5</sub> glass exhibited the lowest at 7.5 × 10<sup>-3</sup> S/cm, consistent with experimental findings. Poitras *et al.* a Buckingham-type force field to study the local atomic structures of Li<sub>2</sub>S-SiS<sub>2</sub> in both glassy and crystalline phases [20], with the force field accurately predicting structure factors and radial distribution functions (RDF) compared to experimental results.

Despite these advancements, studying multicomponent systems like Li<sub>2</sub>S-SiS<sub>2</sub>-P<sub>2</sub>S<sub>5</sub> remains challenging [3], particularly due to the complexity in training, learning, and developing effective parameters for classical force fields, given the intricate interactions and charge polarization in these systems. Recently, machine learning force fields (ML-FFs) [21] have emerged, offering DFT-level accuracy with significantly reduced computational demands. For instance, Xu *et al.* developed an ML-FF for Li<sub>7</sub>P<sub>3</sub>S<sub>11</sub> and conducted a pioneering 1-microsecond

simulation [22], revealing the rotation of corner-sharing PS<sub>4</sub><sup>3-</sup> units and its detrimental impact on Li-ion diffusion. Similarly, Huang *et al.* used another ML-FF to quantify Li-ion diffusion in various Li<sub>10</sub>GeP<sub>2</sub>S<sub>12</sub>-type compositions [23]. These recent studies indicated the potential precision and efficiency of ML-FFs in probing the structural and transport properties of SSEs at the atomic level.

In the present study, we have developed an accurate ML-FF based on extensive DFT data to investigate the structural properties and Li ion conductivities in Li-Si-P-S GSEs. Initially, the ML-FF was validated by comparing energies and forces with those from DFT calculations. The ML-FF was then employed to generate glass structures through melt-quench methods, focusing on compositions like 50Li<sub>2</sub>S-50SiS<sub>2</sub>, 67Li<sub>2</sub>S-33P<sub>2</sub>S<sub>5</sub>, 70Li<sub>2</sub>S-30P<sub>2</sub>S<sub>5</sub>, 75Li<sub>2</sub>S-25P<sub>2</sub>S<sub>5</sub>, and 60Li<sub>2</sub>S-32SiS<sub>2</sub>-8P<sub>2</sub>S<sub>5</sub>, those that have been reported on in the literature and therefore those for which experimental data are avaiable. The computed densities of these glasses, lattice parameters of crystalline materials, and elastic moduli demonstrated remarkable consistency between ML-FF and DFT predictions, aligning well with experimental measurements. Further, we used our ML-FF to analyze the short-range order (SRO), primarily the first coordination shell of the glass former of various LiPS and LiSiS glassy phases s P and Si, at 300 K, as well as the Li ion conductivities in them at different temperatures. The radial distribution functions (RDFs), structure factors, and populations of SRO units in all five glass compositions showed good agreement with experimental data and findings from other computational studies. Additionally, we calculated the rotation of SiS<sub>4</sub> and PS<sub>4</sub> tetrahedra around the lithium diffusion path in ternary 60Li<sub>2</sub>S-32SiS<sub>2</sub>-8P<sub>2</sub>S<sub>5</sub> glass at 300 K, uncovering a correlation between anion rotation and lithium diffusion.

## 2.2 Computational Methodology

## 2.1 Density functional theory simulations

In this study, density functional theory (DFT) simulations were conducted to gather data (energy, atomic force, and virial stress) essential for training the machine learning force field (ML-FF). The detailed methodology for developing the ML-FF is discussed in the following section. The Vienna Ab initio Simulation Package [24–26] (VASP) was employed with a plane wave basis set to label structures in the ML-FF training process. The pseudopotentials were generated using

the Projector Augmented Wave (PAW) method, treating 1s<sup>2</sup> for Li, and 1s<sup>2</sup>2s<sup>2</sup>2p<sup>6</sup> for Si, P, and S as core electrons, respectively. The electronic exchange-correction functionals were computed using the PBEsol functional [27], with an energy cutoff of 500 eV for the plane wave basis set. In reciprocal space, a K points mesh based on the Monkhorst-Pack grid approach with 0.5 Å<sup>-1</sup> spacing was applied. The electronic self-consistent field (SCF) calculations were terminated with an energy convergence criterion of 10<sup>-5</sup> eV, ensuring excellent convergence for energy, force, and structures.

## 2.2 Development of machine learning force field

The efficacy of an ML-FF largely depends on the quality and diversity of its training data. For a robust and efficient ML-FF development, the Deep Potential Generator (DP-GEN) was employed on a concurrent learning framework [28,29]. This framework enhances the model's representativeness by continually incorporating DFT data of atomic structures that significantly deviate from accurate DFT results, a method known as labeling. By assessing the maximum force deviation ( $\sigma_f^{max}$ ) among a suite of parallel-trained models, it can be determined whether an atomic configuration should be added to the dataset. Configurations with small deviations ( $\sigma_f^{max} < \sigma_{low}$ ) are deemed less beneficial for learning, while those deviating excessively ( $\sigma_f^{max} > \sigma_{high}$ ) may stray too far from relevant physical trajectories. Therefore, only configurations between  $\sigma_{low}$  and  $\sigma_{high}$  are considered as candidates for the training set. For the amorphous systems studied,  $\sigma_{low}$  and  $\sigma_{high}$  were adjusted to 0.2 and 0.4 eV/Å, respectively.

The initial phase of the DP-GEN training began with a selection of binary, ternary, and quaternary crystalline structures, including Li<sub>2</sub>S, SiS<sub>2</sub>, P<sub>2</sub>S<sub>5</sub>, Li<sub>2</sub>SiS<sub>3</sub>, Li<sub>4</sub>P<sub>2</sub>S<sub>6</sub>, β-Li<sub>3</sub>PS<sub>4</sub>, γ-Li<sub>3</sub>PS<sub>4</sub>, Li<sub>7</sub>P<sub>3</sub>S<sub>11</sub>, Li<sub>7</sub>PS<sub>6</sub>, and Li<sub>10</sub>SiP<sub>2</sub>S<sub>12</sub>. The atomic structures of these phases were obtained from the Materials Project [30] and werethen distorted to generate the initial training set. The set was expanded through MD simulations using iteratively generated ML-FFs under isothermal–isobaric (NPT) and canonical (NVT) ensembles, with pressure ranging from 0 to 100 bar and temperature from 200 to 2000 K. To adequately represent amorphous phases, various amorphous structures were introduced into the training dataset. These structures were generated either by melting and quenching crystalline materials at 1500 K and 300 K, respectively, or by creating randomly packed structures with PACKMOL [31]. The packed

amorphous structures from PACKMOL, created from fundamental units such as PS<sub>4</sub>,  $P_2S_6$ ,  $SiS_2$ , etc., were optimized using the initial ML-FF for subsequent DP-GEN processes. To further improve the model's accuracy in describing mechanical behaviors,  $\pm 10\%$  strain was applied to mimic deformed structures. After 66 iterations, the training set comprised 41,950 structures that were used in the DFT simulations for supercell energies, atomic forces, and virial stresses.

The final ML-FF model features a radial cutoff of 6.0Å, smoothly transitioning from 5.5 Å. Its embedding network architecture consists of a three-layer neural network with neuron counts of 25, 50, and 100 in each layer. Additionally, the fitting network employs a three-layer residual network (ResNet), with each layer containing 120 neurons. After achieving stable accuracy in DP-GEN, the ML-FF underwent an intensive training of four million epochs with the full training set to produce the final ML-FF. The learning rate was set to decrease exponentially from 0.002 to 3.5×10<sup>-8</sup> over four million training steps.

# 2.3 Molecular dynamics simulations

In this study, all MD simulations were executed using the LAMMPS software [32], with a 1 fs timestep and periodic boundary conditions in three dimensions. The temperature and pressure damping constant were set to 0.1 and 1.0, respectively. The Open Visualization Tool (OVITO) [33] was employed for visualization and analysis of the simulation results. After developing the ML-FF potential, theinitial glass structures were generated through a random packing approach. For each composition, five unique initial structures (comprising 4000 to 5000 atoms) were derived from randomly generated configurations. These structures were equilibrated at a temperature of 1700 K for 250 picoseconds, followed by cooling to 300 K at a rate of 5×10<sup>12</sup> K/sec. After reaching 300 K, each structure underwent a 100-picosecond equilibration run in the NPT ensemble.

Firstly, the density and elastic properties were determined of the resulting glass. The density was calculated by averaging the trajectory over 100 ps after equilibration at 300 K. The elastic tensor (C) was computed directly via Hooke's law, which involves calculating the difference in the pressure tensor after applying a specific deformation (or strain) [34]. The stiffness tensor (S) is the inverse of the elastic tensor. Generalized Hooke's law, using Voigt notation, is represented as:

$$\sigma_i = C_{ii}\epsilon_i$$

where  $\sigma$  is the stress tensor [35],  $\epsilon$  is the strain tensor, and i, j are indices ranging from 1 to 6 in Voigt notation. A 1% deformation was selected to ensure the calculations remained within the linear elastic deformation region. The bulk modulus (B), shear modulus (G), Young's modulus (E), and Poisson's ratio ( $\nu$ ) were then computed using the Voigt-Reuss-Hill (VRH) approximation, which is the arithmetic mean of the Voigt and Reuss averages. The formulas are as follows:

$$B_V = \frac{C_{11} + C_{22} + C_{33} + 2(C_{12} + C_{13} + C_{23})}{9}$$

$$G_V = \frac{C_{11} + C_{22} + C_{33} - (C_{12} + C_{13} + C_{23}) + 3(C_{44} + C_{55} + C_{66})}{15}$$

$$B_R = \frac{1}{S_{11} + S_{22} + S_{33} + 2(S_{12} + S_{13} + S_{23})}$$

$$G_R = \frac{15}{4(S_{11} + S_{22} + S_{33}) - 4(S_{12} + S_{13} + S_{23}) + 3(S_{44} + S_{55} + S_{66})}$$

The Young's modulus and Poisson's ratio were then derived using [36]:

$$E = \frac{1}{\frac{1}{3G} + \frac{1}{9B}}$$

$$v = \frac{1}{2} \left( 1 - \frac{3G}{3B + G} \right)$$

The conductivity of Li ions was calculated by the Nernst-Einstein relation, given as follows:

$$\sigma = n_0 \frac{e^2}{k_B T} D$$

where  $\sigma$  is the ionic conductivity,  $n_0$  is the number of charge-carrier atoms per volume, e is the charge of an electron,  $k_B$  is the Boltzmann constant, T is the temperature, and D is the diffusion coefficient. The diffusion coefficient is calculated from the mean square displacement (MSD) of Li derived from MD simulations:

$$D = \frac{1}{6t} \frac{1}{N} \sum_{i}^{N} [r_i(0) - r_i(t)]^2$$

where t is time, N is the number of all Li atoms, and  $r_i$  is the position of ith Li atom at time 0 and time t.

Li-MSD computations were conducted across a temperature range of 300 to 650 K, at 50 K intervals, using the NPT ensemble. The activation energies for Li ion diffusion were obtained by fitting the diffusion coefficient data to the Arrhenius equation. Simulation durations varied with temperature: 1 ns for temperatures above 400 K, 5 ns at 350 K, and 15 ns at 300 K, to ensure MSD calculation convergence at lower temperatures.

For investigating the structural properties of the amorphous phases, both partial and total radial distribution functions and the neutron structure factor were calculated. The partial structure factors  $S_{ij}(Q)$  are first derived from the partial radial distribution function  $g_{ij}(r)$  as:

$$S_{ij}(Q) = 1 + \rho \int_0^\infty 4\pi r^2 \left(g_{ij}(r) - 1\right) \frac{\sin Q r}{Qr} dr$$

where  $\rho$  is the number density, i and j are atom types. The total neutron structure factors S(Q) is defined as:

$$S(Q) = \sum_{i,j} c_i c_j b_i b_j (S_{ij}(Q) - 1)$$

where  $c_i$  and  $c_j$  are the atomic fractions of atom types i and j,  $b_i$  and  $b_j$  are the coherent scattering lengths for atom types i and j. The values for Li, Si, P, and S are -1.90 fm, 4.15 fm, 5.13 fm, and 2.85 fm, respectively.

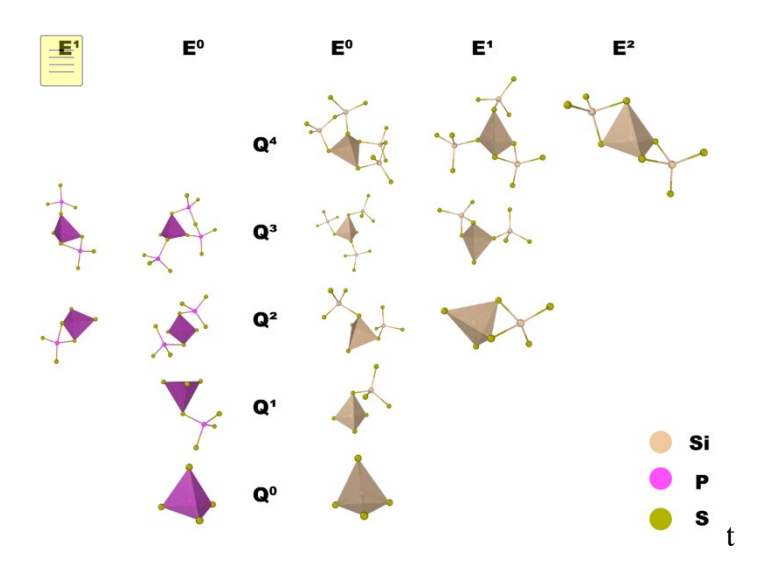


**Figure 1**. Characterizing Si and P local environments using Q<sup>n</sup> and E<sup>n</sup> structural order parameters. The centered atoms are Si (light yellow) or P (light red) surrounded by S atoms (light green).

In analyzing the local structural environment of Si and P within the glass phases, the various SRO Si and P strucfrures were classified based on the number of BS atoms within the Si or P tetrahedra (Si<sup>n</sup> or P<sup>n</sup>) and the number of edge-sharing tetrahedra (E<sup>n</sup>), as illustrated in Figure 1 [10,37]. Si<sup>n</sup> and Pndenotes the number of bridging S atoms connected to a central tetrahedral cation (P or Si), with Si<sup>0</sup> and P<sup>0</sup> indicating an isolated tetrahedron and Si<sup>1</sup> and P<sup>1</sup> a tetrahedron bonded to one BS atom. E<sup>n</sup> quantifies edge-sharing tetrahedral cations in a cluster, with E<sup>1</sup> indicating a single edge-sharing tetrahedron and E<sup>2</sup> two edge-sharing tetrahedra. To determine connectivity within the Si, P, and S atom network, a cutoff distance of 2.6 Å was used, as determined by the RDF results, to include first neighbor bonding interactions.

#### 3. Results and Discussion

## 3.1 Validation of the ML-FF

To demonstrate the accuracy of the ML-FF, the structural and mechanical properties of selected crystalline and amorphous phases were calculated and compared with results from DFT simulations and experimental measurements. Firstly, the fidelity of the ML-FF was benchmarked against DFT values from the training set. As depicted in Figure 2, the energy and force predictions made by the ML-FF closely align with DFT values for all four systems studied: Li<sub>2</sub>S-SiS<sub>2</sub> glass, Li<sub>2</sub>S-SiS<sub>2</sub>-P<sub>2</sub>S<sub>5</sub> glass, and the crystalline Li<sub>10</sub>SiP<sub>2</sub>S<sub>12</sub>. The root-mean-square (RMS)

errors for energies per atom and forces in these systems are 7.57 meV/atom and 0.17 eV/Å, respectively. Notably, this level of accuracy falls slightly short of that achieved by previous ML-FFs for crystalline batteries [22,23]. This slightly less accurate result here is likely due to the inherent variability in the substantially larger datasets of amorphous structures compared to crystalline systems.

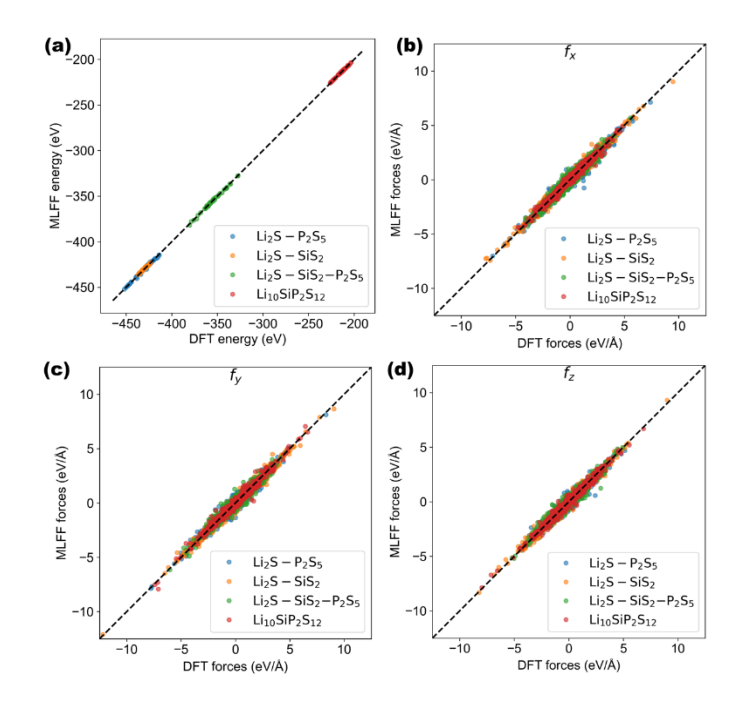


**Figure 2**. ML-FF versus DFT energies and axial forces (fx, fy, fz) for the randomly selected structures from three glassy structures and one crystalline phase.

Next, the lattice parameters and volume of crystalline Li<sub>10</sub>SiP<sub>2</sub>S<sub>12</sub> were compared. Table 1 presents this comparison of the lattice parameters for crystalline Li<sub>10</sub>SiP<sub>2</sub>S<sub>12</sub> as determined by the ML-FF at 300 K, alongside results from both experimental measurements at room temperature [38] and DFT calculations at 0 K [23]. It is worth noting that DFT predicted lattice parameters (or volume) of the unit cell are influenced by the choice of exchange-correlation functionals, with results from the PBEsol functional match best with experimental data. When compared to experimental values at room temperature, the discrepancies in lattice parameters from our ML-FF are less than 1%. The volume predicted by the ML-FF is slightly higher than predicted by PBEsol due to the temperature difference.

**Table 1** Lattice constants and unit cell volume for crystalline Li<sub>10</sub>SiP<sub>2</sub>S<sub>12</sub> obtained from various DFT approaches [23], experimental work [39] and our ML-FF

Method	a (Å)	b (Å)	c (Å)	Volume (Å <sup>3</sup> )
PBE	8.774	8.774	12.599	970.0
PBE + vdw	8.700	8.700	12.490	945.5
LDA	8.534	8.534	12.144	884.3
PBEsol	8.696	8.696	12.368	935.3
SCAN	8.728	8.728	12.496	951.9
PBEO	8.722	8.722	12.518	952.3
Expt.	8.651	8.651	12.5095	936.3
This work	8.695	8.695	12.5104	945.9

It is important to accurately predict the density for describing dynamic properties of GSEs, as lower densities may allow additional free space for anion rotations and Li ion diffusion, consequently leading to substantially higher conductivities [3,40]. A comparative analysis of the density of LPS glass was conducted with both experimental and other computational results for Li<sub>2</sub>S ratios ranging from 67% to 75%. Table 2 lists densities of various LPS glass phases as predicted by the ML-FF, experimental measurements [5,41], DFT-Molecular Dynamics (DFT-MD) predictions [38] and classical force field molecular dynamics (CMD) [19]. The ML-FF predictions agree very well with experimental values, exhibiting a deviation of only within 3%. The accuracy of the ML-FF is similar to DFT simulations and surpasses the results from CMD [19]. It was observed that the density of LPS glass decreases as the Li<sub>2</sub>S concentration increases from 67% to 75%, a trend that is well supported by experimental data. In contrast, CMD models predict a uniform density across all compositions, whereas (DFT-MD) simulations indicate a peak density at a 70% Li<sub>2</sub>S concentration.

**Table 2** Density values of amorphous LPS phases produced by different techniques.

	Li <sub>2</sub> S (%)	this	CMD [19]	Expt. [19]	DFT [42]
--	-----------------------	------	----------	------------	----------

67	1.89	1.84	1.95	1.882
70	1.88	1.84	1.91	1.889
75	1.85	1.84	1.88	1.800

In the final part of this sub-section, the modulus of various glass phases weew examined. Table 3 presents the bulk modulus (B), shear modulus (G), Young's modulus (E), and Poisson's ratio (v) for the four types of systems studied here: Li<sub>2</sub>S-SiS<sub>2</sub> glass, Li<sub>2</sub>S-P<sub>2</sub>S<sub>5</sub> glass, Li<sub>2</sub>S-SiS<sub>2</sub>-P<sub>2</sub>S<sub>5</sub> glass, and the crystalline Li<sub>10</sub>SiP<sub>2</sub>S<sub>12</sub>. These values, as determined by the ML-FF, are compared with experimental measurement and other simulation results [20,43]. Specifically, for the binary Li<sub>2</sub>S-SiS<sub>2</sub> (LiSiS) glass, the ML-FF calculations tend to underestimate the modulus by about 25%, yielding values of B = 19.42 GPa, E = 23.82 GPa, and G = 9.19 GPa for a 50% Li<sub>2</sub>S composition. However, these results align more closely to experiments than those obtained from CMD [20]. As the Li<sub>2</sub>S concentration increases from 50% to 67%, the elastic modulus increases, indicating enhanced mechanical properties with higher Li<sub>2</sub>S content in the LiSiS glass phase. The Poisson's ratio is consistent from both theory and experiment.

For binary Li<sub>2</sub>S-P<sub>2</sub>S<sub>5</sub> (LPS) glasses, the ML-FF predictions agree well with experimental measurements across all three compositions, with most elastic modulus deviating within 20% of experimental values. Similar to LiSiS, the elastic moduli increase with rising Li<sub>2</sub>S concentration according to the ML-FF predictions. However, experimental results do not exhibit a comparable trend, which could be attributed to the fact that the measurements were conducted by different research groups. Additionally, the moduli of LPS were found to be lower than those of Li<sub>2</sub>S-SiS<sub>2</sub> glass at the same Li<sub>2</sub>S concentration (67%), likely due to weaker bonding between P and S compared to Si and S [20,43].

To the best of our knowledge, there are no existing elastic data in literature for the ternary Li<sub>2</sub>S-SiS<sub>2</sub>-P<sub>2</sub>S<sub>5</sub> glass system. The ML-FF predicts values of B = 19.87 GPa, E = 24.19 GPa and G = 9.33 GPa, which lie intermediate between the Li<sub>2</sub>S-SiS<sub>2</sub> and Li<sub>2</sub>S-P<sub>2</sub>S<sub>5</sub> binary systems. This suggests that mechanical stability of ternary glass is similar to binary systems as a small amount of P<sub>2</sub>S<sub>5</sub> is added. Regarding the crystalline Li<sub>10</sub>SiP<sub>2</sub>S<sub>12</sub>, when comparing the present results with DFT calculations using the PBEsol functional [43], values of B = 24.95 GPa, E = 27.74 GPa and

G = 10.55 GPa were observed, with an approximate error margin of 10%. Although the ML-FF is developed for the glass phases, it also provides a good description for crystalline phases.

From these results, it is noted that there is an increase in the Åelastic moduli with rising Li<sub>2</sub>S content, whereas the density decreases with the increasing Li<sub>2</sub>S concentration. This inverse correlation between elastic modulus and density is consistent with experimental findings [6,15]. As the Li<sub>2</sub>S percentage increases, the primary anionic components in the glass changes from chain structures in low Li<sub>2</sub>S glass to more isolated SiS<sub>4</sub><sup>4-</sup> or PS<sub>4</sub><sup>3-</sup> units, resulting in a reduced mean atomic volumes and lower density [6]. These structure changes will be discussed in the following subsections.

**Table 3** Calculated bulk modulus (B), shear modulus (G), Young's modulus (E) and Poisson's ratio (v) from ML-FF and the comparison with other data source (experiments [5,6,4], classical force field molecular dynamics (CMD) [20] and DFT [43]).

	System		Method	В	E	$\mathbf{G}$	v
				(GPa)	(GPa)	(GPa)	
Glass	Li <sub>2</sub> S-SiS <sub>2</sub>	50-50	This work	19.42	23.82	9.19	0.30
			CMD [20]	50.33	58.52	22.40	0.31

			Expt. [6]	26.10	31.00	11.90	0.30
		67-33	This work	23.64	28.27	10.87	0.30
	Li <sub>2</sub> S-P <sub>2</sub> S <sub>5</sub>	67-33	This work	14.98	18.41	7.11	0.30
			Expt. [6]	20.70	22.10	8.40	0.31
		70-30	Thiswork	16.66	20.18	7.77	0.30
			Expt. [5]	19.70	21.90	8.30	0.32
		75-25	This work	18.61	21.89	8.39	0.30
			Expt. [41]	20.90	22.90	8.70	0.32
	Li <sub>2</sub> S-SiS <sub>2</sub> -	60-32-08	This work	19.87	24.19	9.33	0.30
	$P_2S_5$						
Crystal	Li <sub>10</sub> S	SiP <sub>2</sub> S <sub>12</sub>	This work	24.95	27.74	10.55	0.31
			DFT [43]	27.80	24.80	9.20	0.35

# 3.2 Glassy structure and Li ionic conductivity of binary 50Li<sub>2</sub>S-50SiS<sub>2</sub> system

For LiSiS glass, the binary composition 50Li<sub>2</sub>S-50SiS<sub>2</sub> system was the focus of the study and the glassy structure and Li ion conductivity were examined. Figure 3 displays the total, Figure 3(a), and partial, Figure 3(b), radial distribution functions (RDF) from the ML-FF MD simulations, and the comparison with experimental measurement [11] and other simulations using CMD [20]. In Figure 3(a), the three most pronounced peaks correspond to Si-S (2.1 Å), Li-S (2.46 Å), and S-S (3.54 Å) bond correlations and these align well with experimental findings. Notably, however, this agreement in predictions and experimental results diverge at the peak around ~2.8 Å, which is absent in the ML-FF RDF; this discrepancy will be discussed later. Figure 3(b) reveals that while the Si-S and S-S partial RDFs closely match the CMD, significant differences arise in the Si-Si and Li-Si correlations. Specifically, the ML-FF results indicate a peak at 2.8 Å for the Si-Si partial RDF, in contrast to Poitras's identification of a peak at 4.0 Å [20], suggesting that the ML-FF glass network features edge-sharing Si units [10,11]. This variance could explain the trough observed between 2.5 to 3.0 Å in the total RDF. For Li-Si, the ML-FF predicts a boarder peak spanning 3.1 to 3.7 Å, whereas CMD results show a relatively sharper peak at 3.8 Å. The ML-FF partial RDF indicates a Si-Si peak at 2.8 Å, aligning with experimental findings. However, this

peak does not appear in the total RDF, possibly because its relatively low intensity is overshadowed by neighboring peaks such as Li-S (2.46 Å) and S-S (3.54 Å).

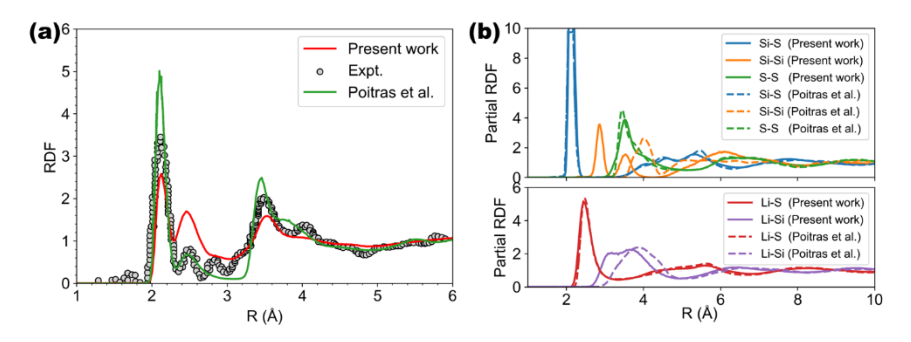


**Figure 3**. The RDFs from ML-FF and compared to previous experimental results [11] and CMD simulations [20]: (a): total RDF; (b) partial RDF.

To gain deeper insight into local atomic structures, the distribution of BS on Si-S units (Si<sup>n</sup> and P<sup>n</sup>) and edge-sharing Si-S units (E<sup>n</sup>) were calculated and are presented in Table 4. Overall, the BS units identified by the ML-FF are consistent with experimental findings and CMD predictions. Notably, the ML-FF data predominantly features Si<sup>2</sup> or Si<sup>3</sup> bridging sulfur units, while CMD results indicate a more even distribution amounts of Si<sup>1</sup>, Si<sup>2</sup>, and Si<sup>3</sup> units. However, in contrast to the 50% occurrence of Si<sup>4</sup> species reported in experiments, our ML-FF model identifies only 1.1% Si<sup>4</sup> species, and CMD predicts 5.8%. The discrepancy in Si<sup>4</sup> representation between the findings of the ML-FF and experimental results could be attributed to two main factors: (1) the minor chemical shifts that make Si<sup>n</sup> identification challenging in experimental results [20]; and (2) differences in simulation parameters, such as quenching rates, which can substantially influence the resulting structures, compared to those produced by experimental ball-milling methods [44].

**Table 4.** Si<sup>n</sup>, P<sup>n</sup>, and E<sup>n</sup> distribution (in 50Li<sub>2</sub>S-50SiS<sub>2</sub> glass from ML-FF and compared with other experiment [11] and classical force field molecular dynamics (CMD) [20].

	$Q^0$	Q <sup>1</sup>	$Q^2$	$Q^3$	Q <sup>4</sup>	$E^0$	$E^1$	E <sup>2</sup>
CMD	7.5	30.6	35.4	20.7	5.8	100		
Expt.			50		50	77	23	
This work	4.2	14.4	59.6	20.6	1.1	34.5	65.2	0.3

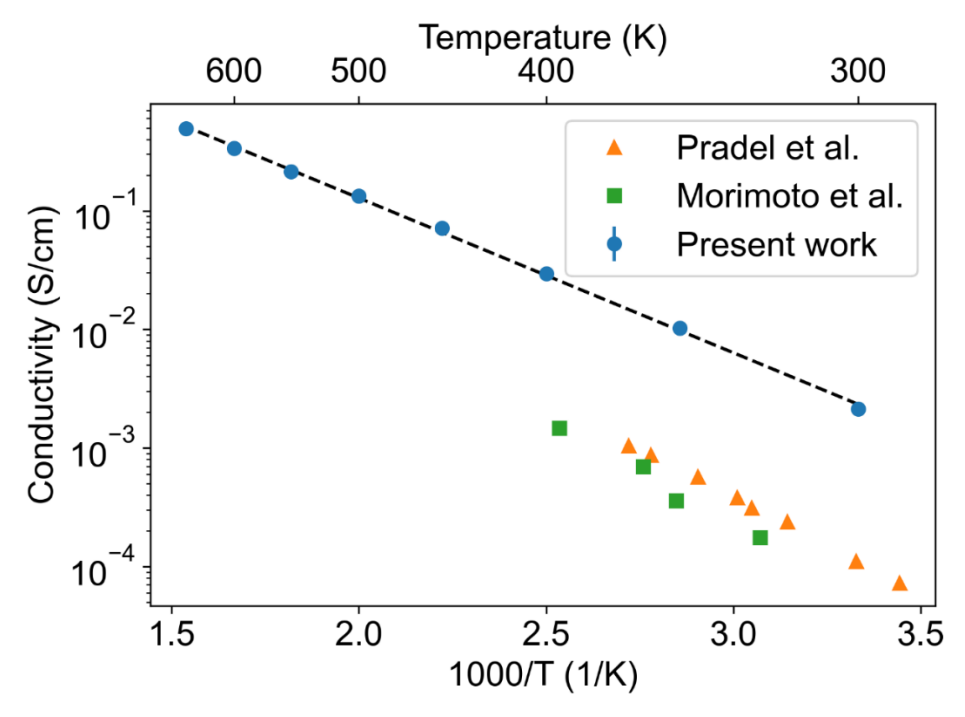
In examining the population of edge-sharing Si (E<sup>n</sup>) clusters, the analysis based on ML-FF simulations reveals a notable presence of 65.2% E<sup>1</sup> and only 0.3% E<sup>2</sup> clusters, as shown in Table 4. This finding contrasts with CMD results, which shows a complete absence of edge-sharing clusters [20], aligning with experimental results. For the composition of the edge-sharing E<sup>1</sup> SRO units of Si, E<sup>1</sup>Si<sup>2</sup> species at 41.9%, E<sup>1</sup>Si<sup>3</sup> species at 19.3%, and E<sup>2</sup>Si<sup>4</sup> species at 0.9% were found. These specific population details are shown in Table 5. The majority of E<sup>2</sup>Si<sup>2</sup> within the edge-sharing category suggests that the 50Li<sub>2</sub>S-50SiS<sub>2</sub> glass maintains a partial chain-like structure, characterized by SiS<sub>4</sub> tetrahedra interconnected via either S-S edges or S corners [20]. These ML-FF findings show a closer alignment with experimental observations than does CMD, particularly in terms of the accurate representation of Si<sup>2</sup> units and the presence of edge-sharing units.

Table 5. Calculated Si<sup>n</sup> and E<sup>n</sup> population (%) in 50Li<sub>2</sub>S-50SiS<sub>2</sub> glass

	$\mathrm{E}^0$	$E^1$	$E^2$
Si <sup>0</sup>	4.8	0	0
$Si^1$	16.9	0	0
$\mathrm{Si}^2$	12.6	41.9	0
$Si^3$	2.9	19.3	0
$\mathrm{Si}^4$	0	0.9	0.8

Figure 4 displays the computed Li ionic conductivity of the  $50\text{Li}_2\text{S}$ - $50\text{SiS}_2$  glass derived from the ML-FF simulations, alongside a comparison with experimental measurements [12,45]. The simulations predict an ionic conductivity of 2.13 mS/cm at 300K ( $\sigma_{300\text{K}}$ ), which is approximately an order of magnitude higher than typical experimental results that are in the  $10^{-4}$  S/cm range. The activation energy ( $\Delta E_{act}$ ) for Li diffusion calculated in the ML-FF study is ~25 kJ/mole, aligning reasonably well with the experimental measurement of 31kJ/mole. Several factors may explain the discrepancies between the experimental results and the ML-FF simulation outcomes [46]. Distinct synthesis techniques, such as melt-quenching and ball milling, can result in varied phases, heterogeneous structures, and the introduction of impurities, all of which significantly influence the resulting conductivity values. Further, the ML-FF simulation models do not include any impurities, and the quenching rate in the ML-FF is much faster, leading to

more homogeneous amorphous structures. Taking these factors into account, the predicted conductivity aligns with the range of experimental measurements. Furthermore, Nernst-Einstein equation was used to estimate ionic conductivity, assuming that ion interactions do not influence conductivity. This assumption may also contribute to the observed discrepancies between theoretical predictions and experimental results.



**Figure 4**. The conductivity of 50Li<sub>2</sub>S-50SiS<sub>2</sub> glass predicted from ML-FF simulations, and the comparison with experimental measurements [12, 45].

## 3.3 Glassy Structure and ionic conductivity of binary Li<sub>2</sub>S-P<sub>2</sub>S<sub>5</sub> system

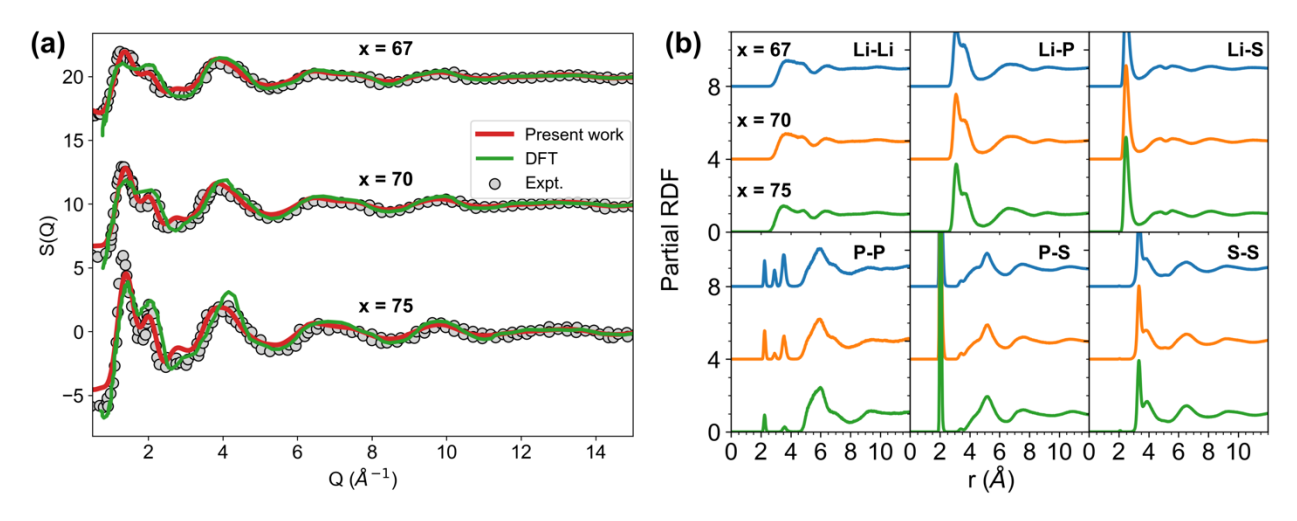


**Figure 5**. (a) Neutron structure factor (S(Q)) and (b) partial RDFs for three binary  $xLi_2S$ -(100- $x)P_2S_5$  glasses (x = 67, 70, 75).

In this study, we examined the binary LPS glass with three different Li<sub>2</sub>S concentrations, specifically  $xLi_2S$ -(100-x)P<sub>2</sub>S<sub>5</sub> where x is 67, 70 and 75. Notably, the Li ion conductivity of 75Li<sub>2</sub>S-25P<sub>2</sub>S<sub>5</sub> has been reported to be as high as 0.3 - 1.0 mS/cm [15,47]. Figure 5(a) shows the neutron structure factor, S(Q), for these three compositions, compared with previous experimental and DFT-MD results [15]. The S(Q) of the glassy structure derived from the ML-FF simulations shows remarkable agreement across the entire range with existing experimental data, surpassing even the DFT-MD results. The intensity of the first principal peak, located at around Q = 1.4 Å<sup>-1</sup>, aligns well for x=67 and x=70 compositions, but slightly underestimate for x=75. The first peak is due to intermediate range order of Li-P, P-P, and P-S, corresponding to a periodicity of 4.5 Å. The second and third principal peaks, observed at 2.0 Å<sup>-1</sup> and 3.8 Å<sup>-1</sup>, are also reproduced with high accuracy. The second peak corresponds to S-S periodicity and the third peak is associated with both S-S and P-S short-range periodicities.

Figure 5(b) shows the partial pair distribution functions (RDFs) for Li-Li, Li-S, Li-P, P-P, P-S and S-S. While there is a broad consensus between the three components, certain disparities, particularly in the P-P pair correlation, emerge. Typically, two peaks are observed in the P-P correlation: one at 2.2 Å representing the direct bonding in the  $P_2S_6^{4-}$ , and another at 3.5 Å for the

corner-sharing P<sub>2</sub>S<sub>7</sub><sup>4-</sup> clusters. An analysis of these results reveals an additional peak at 2.9 Å for x=67 and x=70. This peak is indicative of the P-P distance in the edge-sharing P<sub>2</sub>S<sub>6</sub><sup>2-</sup> clusters. In the Li-Li RDF, the first peak for x=75 is slightly shifted towards smaller distances, positioned at 3.5 Å, compared to 3.7 Å in both x=67 and x=70. The Li-P RDF shows the first peak at 3.1 Å, while the P-S RDF has its first peak at 2.0 Å, indicating the P-S bonds in the local clusters, such as PS<sub>4</sub> tetrahedra. The Li-S and S-S RDFs remain relatively consistent across all three compositions. The Li-S and S-S RDFs remain relatively consistent across all compositions, with the Li-P RDF showing the first peak at 2.5 Å and the S-S RDF's first and second peaks observed at 3.3 Å and 3.9 Å, respectively. These S-S peaks correspond to the S-S distances in inter- and intra-PS molecular clusters [16].

Detailed results for bridging sulfur (P<sup>n</sup>) and the edge-sharing phosphorus (E<sup>n</sup>) are tabulated in Table 6. Usually the edge-sharing unit in the LPS glass is considered less likely to form compared to LiSiS glass, especially when Li<sub>2</sub>S is over 50% [10]. However, the ML-FF simulated glass structures contain 16.9% and 9.6% edge-sharing P<sub>2</sub>S<sub>6</sub><sup>2-</sup> units, indicated by E<sup>1</sup> in Table 6, for 67% and 70% Li<sub>2</sub>S, respectively. Despite variations in the exact populations, the ML-FF simulated glass structures reveal that the populations of corner-sharing P<sub>2</sub>S<sub>7</sub><sup>4-</sup>, P-P dimer P<sub>2</sub>S<sub>6</sub><sup>4-</sup>, and edge-sharing P<sub>2</sub>S<sub>6</sub><sup>2-</sup> decrease with an increase in Li<sub>2</sub>S percentage, while the population of PS<sub>4</sub><sup>3-</sup> rises. Particularly, the corner-sharing P<sup>1</sup> (P<sub>2</sub>S<sub>7</sub><sup>4-</sup>) percentage changes from 26.3% to 20.8% and then to 6.82% as the Li<sub>2</sub>S percentage increases from 67% to 70% and to 75%. This trend aligns with experimental results. The rising population of isolated PS<sub>4</sub> tetrahedra indicates a reduced mean atomic volume, which may account for the increased elastic modulus [6].

**Table 6.** Q<sup>n</sup> and E<sup>n</sup> distribution (%) in three  $xLi_2S$ -(100-x)P<sub>2</sub>S<sub>5</sub> glasses (x = 67, 70, 75) from ML-FF simulations.

Li <sub>2</sub> S		P	n		F	En
percentage						
X	$P^0$	$P^1$	$P^2$	$P^3$	$E^0$	$E^1$
67	50.1	26.3	21.5	2.1	83.1	16.9
70	67.6	20.8	11.3	0.3	90.4	9.6
75	93.2	6.8	0.0	0.0	100	0

The computed conductivities for the x=67, x=70, and 75 GSEs are 2.2 mS/cm, 2.9 mS/cm, and 3.6 mS/cm, respectively, which align well with other computational [17,19] and experimental [15,48,49] findings, as shown in Figure 6(a). The calculated diffusion activation energies for these compositions are 0.313 eV, 0.307 eV, and 0.303 eV, respectively, which are also consistent with experimental and computational results (Figure 6(b)). It was suggested that the presence of P<sub>2</sub>S<sub>7</sub><sup>4-</sup> anion could suppress lithium ionic conduction [15] due to stronger attraction between P<sub>2</sub>S<sub>7</sub><sup>4-</sup> and Li<sup>+</sup>. This is consistent with our predictions on Li ionic conductivity in Figure 6 and P<sup>n</sup> populations in Table 6. The calculations of the P<sup>n</sup> species show a significant decrease in P<sup>1</sup>~P<sup>3</sup> and drastic increase in Q<sup>0</sup> as Li<sub>2</sub>S concentration increases from 67% to 75%. This explains the highest conductivity of 75Li<sub>2</sub>S-25P<sub>2</sub>S<sub>5</sub> among all three compositions. It is worth noting that that the ionic conductivity from ML-FF and other theoretical studies are much higher than experimental measurements. Indeed, the ML-FF predictions show less discrepancy compared with other theoretical studies. The discrepancy between theory and experiment may arises from the relatively low glass forming ability in binary LPS and the experimental samples consist of impurity and heterogeneous structures.

The ionic conductivity is related to the diffusion process of Li in the binary glass. When comparing the calculated diffusion coefficients, which stand at  $2.51 \times 10^{-8}$  cm<sup>2</sup>/s for x=67, 2.96  $\times 10^{-8}$  cm<sup>2</sup>/s for x=70, and  $3.16 \times 10^{-8}$  cm<sup>2</sup>/s for x=75, the difference in diffusion coefficients between x=75 and x=70 is less than that between x=70 and x=65. This is notable since the difference in P<sup>n</sup> species between x=75 and x=70 is greater than that between x=70 and x=67. This suggests that the effect of  $P_2S_7^{4-}$  is not linear and its effects on the Li diffusion significantly increases as P<sup>1</sup> specie concentration increases to 26.3%. It is worth mentioning that other factors such as the number density of Li could also attribute to the overall conductivity [42] and a higher Li number density in x=75 composition may enhance the Li ionic conductivity. Similar to ionic conductivity, the activation energy predicted from theory is systematically lower than experimental measurements.

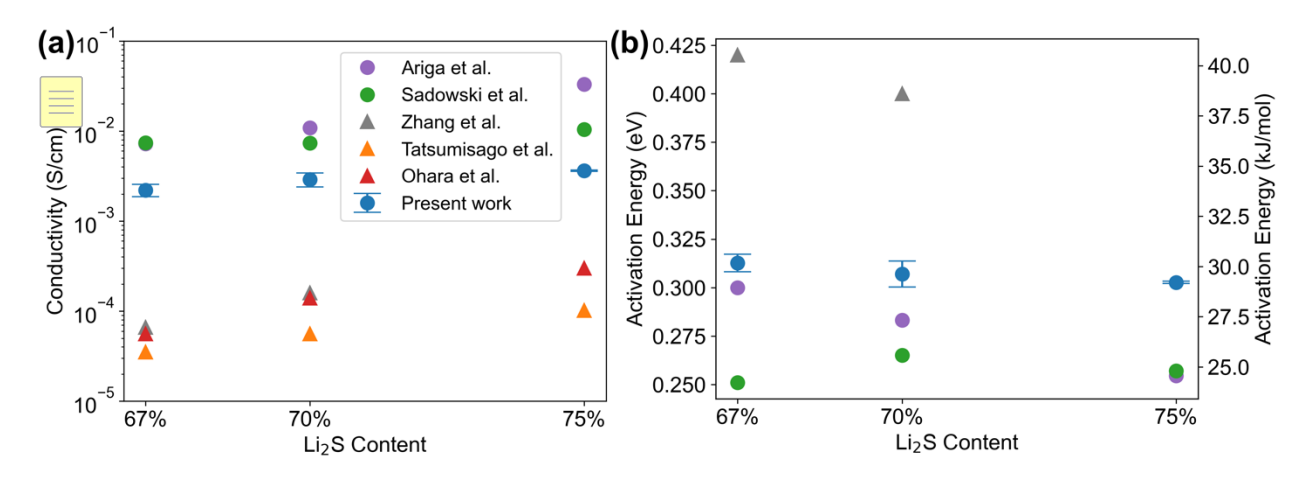


**Figure 6**. The ML-FF predicted (a) ionic conductivities at room temperature and (b) activation energies for three  $xLi_2S-(100-x)P_2S_5$  glasses (x = 67, 70, 75), and the comparison with experimental [2,15,48] and other theoretical [17,19] studies.

# 3.4 Structure and ionic conductivity of ternary 60Li<sub>2</sub>S-32SiS<sub>2</sub>-8P<sub>2</sub>S<sub>5</sub> glass

The ternary Li<sub>2</sub>S-SiS<sub>2</sub>-P<sub>2</sub>S<sub>5</sub> glass exhibits several advantages over its binary counterparts, Li<sub>2</sub>S-SiS<sub>2</sub> and Li<sub>2</sub>S-P<sub>2</sub>S<sub>5</sub>. The binary Li<sub>2</sub>S-SiS<sub>2</sub> glass demonstrates instability when in contact with lithium metal, which limits its application in all-solid-state batteries. The synthesis of Li<sub>2</sub>S-P<sub>2</sub>S<sub>5</sub> is challenging due to the high vapor pressure of P<sub>2</sub>S<sub>5</sub> [14]. In contrast, the ternary Li<sub>2</sub>S-SiS<sub>2</sub>-P<sub>2</sub>S<sub>5</sub> glass composition shows enhanced stability against lithium metal, with P<sub>2</sub>S<sub>5</sub> acting as a stabilizer [50]. This glass also exhibits improved glass-forming ability, facilitating the production of homogeneous bulk glasses devoid of heterogeneities and phase boundaries [14]. Previous study showed that among the 60Li<sub>2</sub>S-40[(1-x)SiS<sub>2</sub>-xP<sub>2</sub>S<sub>5</sub>] compositions, the variant 60Li<sub>2</sub>S-32SiS<sub>2</sub>-8P<sub>2</sub>S<sub>5</sub> exhibits the highest conductivity at 0.7 mS/cm at room temperature [13]. In this work, we investigate the structural properties and lithium-ion conductivity of the 60Li<sub>2</sub>S-32SiS<sub>2</sub>-8P<sub>2</sub>S<sub>5</sub> compound, aiming to gain a deeper understanding of its efficacy as a solid electrolyte.

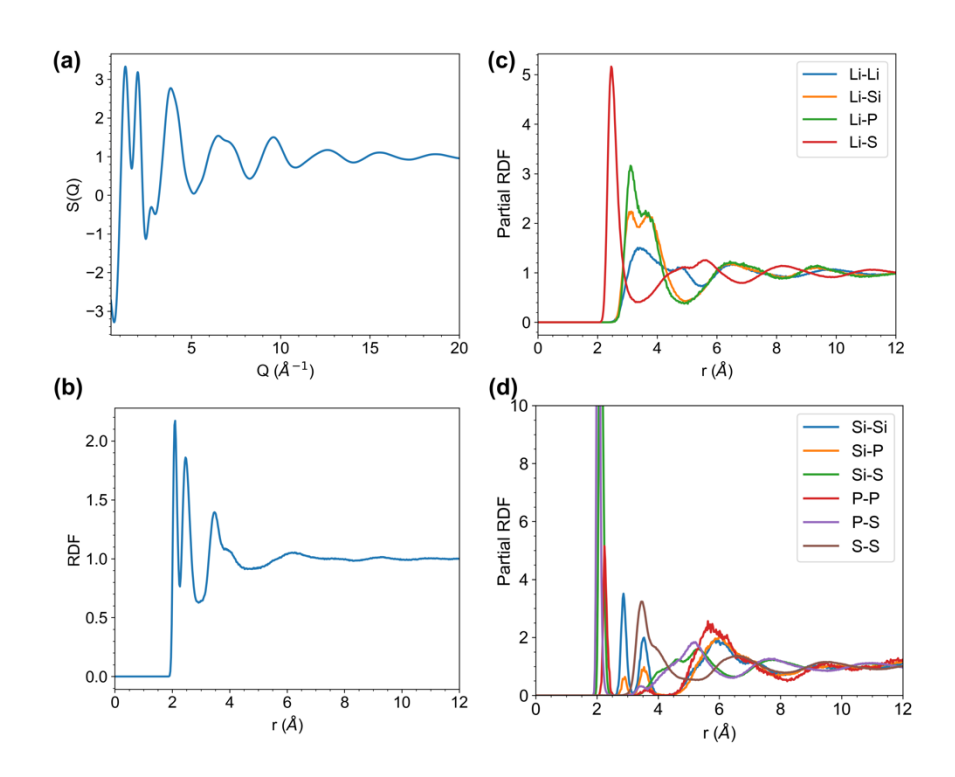


**Figure 7**. (a) Neutron structure factor (S(Q)), (b) radial distribution function (RDF), and (c, d) partial radial distribution functions for the 60Li<sub>2</sub>S-32SiS<sub>2</sub>-8P<sub>2</sub>S<sub>5</sub> glass, as derived from ML-FF simulations at room temperature.

To best of our best knowledge, there have been no experimental or computational studies reporting the RDF or neutron structure factor, S(Q), for the ternary  $60Li_2S-32SiS_2-8P_2S_5$  glass system. Figure 7(a) shows the computed S(Q) for the  $60Li_2S-32SiS_2-8P_2S_5$  glass from the ML-FF simulations. The first peak, appearing at around 1.3 Å<sup>-1</sup>, is attributed to the Si-S network. The second and third peak, located at  $\sim 2.0$  Å<sup>-1</sup> and 3.8 Å<sup>-1</sup>, corresponds to S-S interactions and short-range order involving S-S, P-S, and Si-S, respectively. Figure 7(b) illustrates the total RDF for this ternary glass, marked by three significant peaks. The first peak at 2.1 Å is predominantly due to P-S (2.05 Å) and Si-S (2.1 Å) bonds. The subsequent peaks at 2.46 Å and 3.46 Å are indicative of Li-S and S-S bonds, respectively. Figure 7(c) depicts the Li partial RDF, where the Li-Si RDF reveals two peaks at 3.1 Å and 3.7 Å, similar to our findings in the binary  $50Li_2S-50SiS_2$  glass.

The P-P partial RDF, shown in Figure 7(d), presents a strong peak around 2.2 Å and a weaker peak around 3.6 Å, indicating the presence of the P-P bond  $(P_2S_6^{4-})$  unit and a low amount of corner-sharing  $P_2S_7^{4-}$  unit, with no edge-sharing  $P_2S_6^{2-}$  unit. This agrees well with the MAS-NMR

experimental data [14]. Moreover, Figure 7(d) indicates that Si-Si and Si-P peaks are at 2.9 Å and 3.5 Å, suggesting the coexistence of edge-sharing and corner-sharing SiS<sub>4</sub> and PS<sub>4</sub> tetrahedral units within the glass. However, no peaks are observed around 2.2 Å for the Si-Si RDF, indicating no Si-Si bonds, normally observed in Si<sub>2</sub>S<sub>6</sub><sup>6</sup>- units, are present in our simulated ternary glass. This finding contrasts with MAS-NMR experimental data [14], which suggested the presence of 35.7% Si<sub>2</sub>S<sub>6</sub><sup>6</sup>-. Additionally, these experimental results indicated that 66.0% of phosphorus and 32.8% of silicon exist as isolated PS<sub>4</sub> and SiS<sub>4</sub> tetrahedral clusters, respectively. These isolated tetrahedral units are consistent with the first peaks in partial P-S and Si-S RDFs.

**Table 7.** Si<sup>n</sup> and E<sup>n</sup> distribution (%) in 60Li<sub>2</sub>S-32SiS<sub>2</sub>-8P<sub>2</sub>S<sub>5</sub> glass from ML-FF and the comparison with experiment [14].

			Si <sup>n</sup> , P <sup>n</sup>					En	
	n	0	1	2	3	Q44	E0	E1	E2
Experiment	Si	70.2	5.1	22.7	2.0	0	83.0	17.0	0
	P	85.9	14.0	0	0	0	100	0	0
This work	Si	20.2	25.3	44.2	9.8	0.5	58.4	41.3	0.3
	P	69.8	21.3	8.4	0.6	0	94.3	5.7	0

**Table 8.** Detailed local environment of P in 60Li2S-32SiS2-8P2S5 glass from ML-FF

n = # of BS	# of Edge-sharing	P-S-X	P-X	Population
(P <sup>n</sup> )	units (E <sup>n</sup> )			
0	0			60.8%
0	0		P	9.0%
1	0	Si		16.8%
2	1	Si, Si		5.0%

Table 9. Detailed local environments of Si in 60Li2S-32SiS2-8P2S5 glass from ML-FF

n=# of BS (Si <sup>n</sup> )	# of Edge-sharing units (E <sup>n</sup> )	Si-S-X	Population
0	0		20.2%
1	0	Si	21.7%
2	0	Si, Si	7.9%
2	1	Si, Si	29.5%

To further investigate the local environments of P and Si, the dominant local SRO units for P and Si are given in Tables 8 and 9. The full data are provided in Table S1 and Table S2. The ML-FF computed fractions of the various P<sup>n</sup> and E<sup>n</sup> SRO units in the simulated glass structure are compared with the <sup>31</sup>P MAS-NMR experimental data [14], and are shown in Table 7. For P related clusters, the ML-FF results reveal a predominant Si<sup>0</sup> at 69.8%. Further examination on E<sup>n</sup> indicates the distribution of P atoms in PS<sub>4</sub><sup>3-</sup> tetrahedron at 60.8% and in P<sub>2</sub>S<sub>6</sub><sup>4-</sup> units at 9.0% (Table 8). The remaining PS<sub>4</sub> tetrahedra are mostly corner-sharing with SiS<sub>4</sub> tetrahedra, where 16.8% P atoms are connected to Si atoms through bridging sulfur, and 3.4% P atoms are connected to P atoms through BSs. The E<sup>1</sup> PS<sub>4</sub> tetrahedra have an even smaller population, accounting for only around 5.7%, and these are predominantly edge-sharing with SiS<sub>4</sub> tetrahedra. The corner-sharing and edge-sharing units connecting SiS<sub>4</sub> and PS<sub>4</sub> are not recognized in previous experimental work [14].

Regarding Si local environments, our ML-FF predicts 44.2% Si<sup>2</sup>, 25.3% Si<sup>1</sup>, and 20.23% Si<sup>0</sup> species. Similar to the 50Li<sub>2</sub>S-50SiS<sub>2</sub> results, the Si<sup>2</sup> species are predominantly edge-sharing units. The non-edge-sharing Si units have a slightly larger population, with E<sup>0</sup> Si at 58.40% and E<sup>1</sup> Si at 41.29%. Like the experiments, E<sup>2</sup> Si is less likely to be found in this glass. The most populated Si environments in our simulated glass are 29.5% in edge-sharing Si<sub>2</sub>S<sub>6</sub><sup>4-</sup>, 21.7% in corner-sharing Si<sub>2</sub>S<sub>7</sub><sup>3-</sup>, and 20.2% in isolated SiS<sub>4</sub><sup>4-</sup>, as shown in Table 9. This is partly consistent with experimental results [14], which claim 32.8% in SiS<sub>4</sub><sup>4-</sup>, and 17.0% in Si<sub>2</sub>S<sub>6</sub><sup>4-</sup>, and 5.1% Si<sub>2</sub>S<sub>7</sub><sup>3-</sup>, respectively. However, there are no Si-Si bonds (Si<sub>2</sub>S<sub>6</sub><sup>6-</sup> units) found in the ML-FF simulated glass, while experimental results show there are 35.7%. This may suggest that the simulated glass structure is primarily composed of a connected SiS<sub>4</sub> network, similar to the 50Li<sub>2</sub>S-50SiS<sub>2</sub> glass, with some Si atoms in the network replaced by P atoms, rather than isolated SiS<sub>4</sub> and PS<sub>4</sub>

tetrahedral clusters. The difference between the ML-FF simulated glass and experimental results could be attributed to fast cooling rates in MD simulations, as well as the different procedure (ball-milling and melt-quenching) of obtaining glass experimentally.

Next, the Li ion conductivity were determined from the ML-FF in this ternary 60Li<sub>2</sub>S-32SiS<sub>2</sub>-8P<sub>2</sub>S<sub>5</sub> glass at relative high temperatures and were compared to the results with existing experimental data [13,14], as illustrated in Figure 8. Due to the limited timescale of MD simulations, the ionic conductivity was computed at high temperatures from 300 to 650 K, whereas the experimental data predominantly pertain to low temperatures from -60 to 90 °C. Overall, the Li ion conductivity predicted using ML-FF aligns closely with experimental findings. Notably, at room temperature, the ML-FF predicts a Li ion conductivity of 2.57 mS/cm, slightly surpassing the experimental values of 1.0 mS/cm [14] and 0.7 mS/cm [13]. Furthermore, the ML-FF predicted activation barrier for Li diffusion is 26.1 kJ/mole eV, modestly lower than the experimental reported values of 30.9 kJ/mole [14] and 34.7 kJ/mole [13]. It is noteworthy that the calculated conductivity for ternary 60Li<sub>2</sub>S-32SiS<sub>2</sub>-8P<sub>2</sub>S<sub>5</sub> glass is comparable to that of the binary 50Li<sub>2</sub>S-50SiS<sub>2</sub> glass (2.17 mS/cm) and the binary LPS glass with a composition of 70Li<sub>2</sub>S-30P<sub>2</sub>S<sub>5</sub> (2.9 mS/cm). This implies that the ternary glass possesses relatively high ion conductivity, suitable for practical applications, and potentially offers superior stability compared to the binary LPS and LiSiS glasses. It is worth noting that the difference between calculated and experimental conductivity in the ternary glass is much less than in the binary glass, which could be attributed to the increased homogeneity of the ternary samples from experiments [13,14].

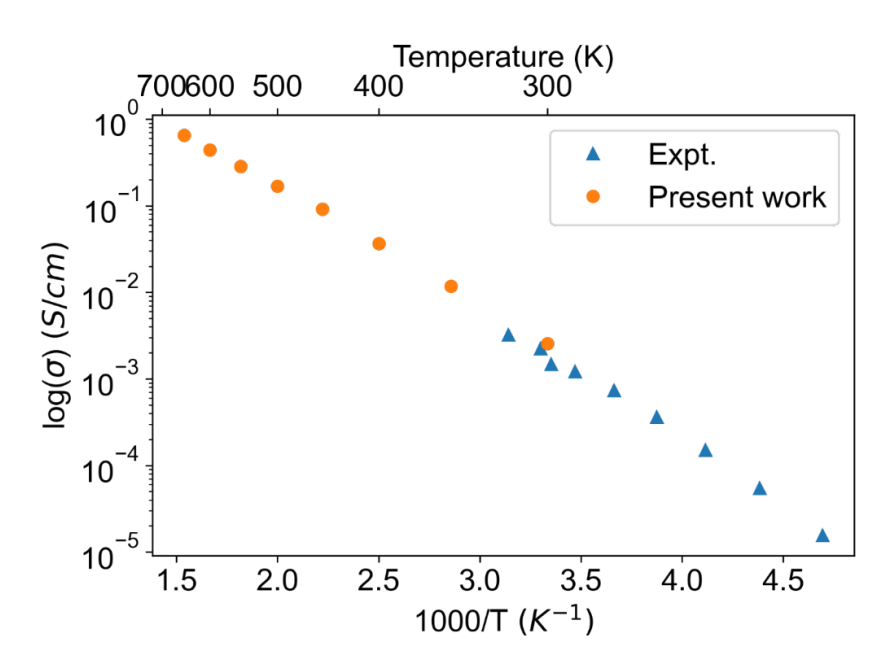


**Figure 8**. Calculated Li ion conductivity from ML-FF and the comparison with experiment results [14].

To elucidate the high ionic conductivity mechanism of this ternary glass, we investigated the Li ion diffusion mechanism at room temperature. Figure 9 displays the atomic structure of the ternary glass structure from ML-FF simulations, along with a detailed view of the trajectories of typical Li-ions over 30 ps at room temperature. These trajectories, illustrated using colored spheres, indicate the beginning (b) and ending (e) positions of six lithium ions. Notably, lithium ions #5, #6, and #10 demonstrate correlated diffusion behavior around tetrahedra A through D. As they migrate out from their initial locations, other lithium ions move in to occupy the positions they vacated. Meanwhile, Li ions #8 follows an uncorrelated diffusion path along the tetrahedra A, and ions #7 and #9 remains near their original locations.

Previous research has suggested that Li cation transport may be associated with the reorientation of neighboring anions clusters in LPS glass [40], leading to a low temperature "paddle-wheel" effect and enhanced Li ion conductivity. However, the lower glass density in those studies might contribute to this effect [3]. In the investigation here, the densities found from ML-FF and experiments agree quite well. For this reason, the potential "paddle-wheel" effect was examined more accurately. This effects was illustrated by analyzing the rotation angles of the tetrahedra using the Kabsch algorithm [51]. The ML-FF findings reveal significant rotations in tetrahedra C,

E, and G (17.3°, 9.7°, and 22.2°, respectively), while tetrahedron D exhibits a smaller rotation of 5.0°. The remaining tetrahedra rotate to a much less degree, generally between 1° and 3°. It is noteworthy that tetrahedra C, E, and G are associated with the correlated diffusion of Li ions #5, #6, and #10, suggesting that tetrahedral rotation might facilitate lithium ion diffusion via the "paddle-wheel" effect, thereby lowering energy barriers [52]. Interestingly, tetrahedron A remains relatively stationary, even as nearby lithium ions move. This finding underscores the need for future research to delve deeper into the underlying mechanisms of the "paddle-wheel" effect and its relationship with nearby lithium diffusion.

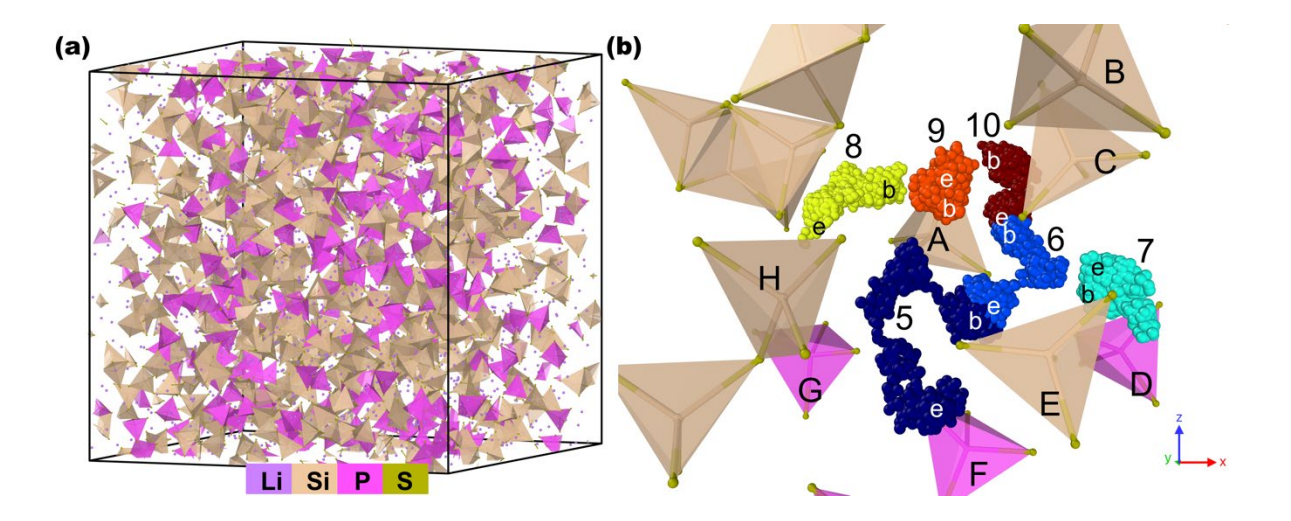


**Figure 9.** (a) Atomic model of  $60\text{Li}_2\text{S}-32\text{SiS}_2-8\text{P}_2\text{S}_5$  glass at room temperature, derived from ML-FF simulations; (b) magnified view of the local structure, highlighting superimposed trajectories of lithium ions over a 30 ps period. The lithium diffusion trajectories are represented by colored spheres, where 'b' denotes the initial lithium position and 'e' marks the end position of diffusion ruing the 30 ps period. PS<sub>4</sub> and SiS<sub>4</sub> tetrahedra are distinguished by purple and brown colors, respectively.

## 4. Conclusions

In summary, a new machine learning force field (ML-FF) has been developed that can be used for a range of lithium sulfide GSEs Initially, the ML-FF was validated against density functional theory (DFT) calculations, demonstrating good agreement in predicted energy and force values. It was then used to generate glass structures which included the compositions

50Li<sub>2</sub>S-50SiS<sub>2</sub>, 67Li<sub>2</sub>S-33P<sub>2</sub>S5, 70Li<sub>2</sub>S-30P<sub>2</sub>S<sub>5</sub>, 75Li<sub>2</sub>S-25P<sub>2</sub>S<sub>5</sub>, and 60Li<sub>2</sub>S-32SiS<sub>2</sub>-8P<sub>2</sub>S<sub>5</sub>, through melt-quench simulations using the developed ML-FF. The lattice parameters of crystalline Li<sub>10</sub>SiP<sub>2</sub>S<sub>12</sub> were also determined to further validate the ML-FF. Our ML-FF accurately predicted density, elastic modulus, RDFs, and neutron structure factors. Following this validation, the ML-FF was used to calculate the local environments of Si and P atoms in these glasses, as well as the Li ionic conductivity from 300 K to 650 K.

For the 50Li<sub>2</sub>S-50SiS<sub>2</sub> glass, the ML-FF successfully identified the edge-sharing units, a feature observed in experiments but not reproduced so-far by classical force fields. Consistent with experiments, it predicts that approximately 65% of Si atoms in this glass exist in an edge-sharing environment. In the Li<sub>2</sub>S-P<sub>2</sub>S<sub>5</sub> glass, the ML-FF suggests a minor presence of edge-sharing P<sub>2</sub>S<sub>6</sub><sup>2-</sup> environments in compositions with 67% and 70% Li<sub>2</sub>S. The P<sup>1</sup> to P<sup>4</sup> species decrease in concentration with increasing Li<sub>2</sub>S content, while the P<sup>0</sup> species increase in concentration, a trend consistent with experimental observations indicating a breakdown of the connected network into isolated units as Li<sub>2</sub>S concentration increases. For the ternary 60Li<sub>2</sub>S-32SiS<sub>2</sub>-8P<sub>2</sub>S<sub>5</sub> glass, the ML-FF accurately predicts P environments but does not identify the Si-Si dimer unit (Si<sub>2</sub>S<sub>6</sub><sup>6-</sup>). Moreover, it indicates the presence of both corner and edge sharing between PS<sub>4</sub> and SiS<sub>4</sub> tetrahedra. These differences highlight that our ML-FF's predictions for the 60Li<sub>2</sub>S-32SiS<sub>2</sub>-8P<sub>2</sub>S<sub>5</sub> structure feature fewer isolated anions compared to experimental data.

Regarding ionic conductivity at 300K, all five glass compositions demonstrate similar magnitudes of conductivity and adhere to the Arrhenius relationship. The 50Li<sub>2</sub>S-50SiS<sub>2</sub> glass exhibits the lowest conductivity at 2.1 mS/cm, while the 75Li<sub>2</sub>S-25P<sub>2</sub>S<sub>5</sub> glass shows the highest at 3.6 mS/cm. The ternary glass records a conductivity of 2.6 mS/cm, placing it in between. The predicted conductivities are approximately an order of magnitude higher than experimental results for the binary Li<sub>2</sub>S-SiS<sub>2</sub> and Li<sub>2</sub>S-P<sub>2</sub>S<sub>5</sub> glasses, but they align closely with the ternary glass. This suggests that the ternary glass may be more homogenous than binary glasses. Further, we analyzed 30-ps Li-ion trajectories within a section of the 60Li<sub>2</sub>S-32SiS<sub>2</sub>-8P<sub>2</sub>S<sub>5</sub> glass. Observations indicate that lithium ions near SiS<sub>4</sub> or PS<sub>4</sub> tetrahedra, exhibiting larger rotations, show more pronounced diffusion compared to those near less rotating tetrahedra. However, it is not a consistent rule that all tetrahedra near diffused lithium ions demonstrate significant rotation.

#### Acknowledgements

This work was supported by the start-up grant from Iowa State University and the simulations were performed at ISU High Performance Computing clusters. Work contributed by SWM was supported in part by the NSF through grant DMR-1936913 and by the DOE through contracts DE-EE0008852 and Battelle Memorial Institute/PNNL subcontract number 679315.

#### References

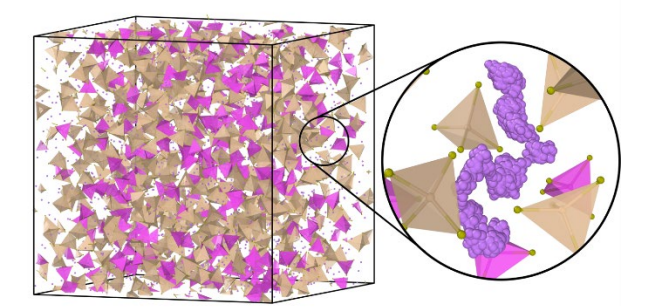
- [1] P. Albertus et al., Challenges for and Pathways toward Li-Metal-Based All-Solid-State Batteries, ACS Energy Lett. 1399 (2021).
- [2] Q. Zhang, D. Cao, Y. Ma, A. Natan, P. Aurora, and H. Zhu, Sulfide-Based Solid-State Electrolytes: Synthesis, Stability, and Potential for All-Solid-State Batteries, Adv. Mater. 31, 1901131 (2019).
- [3] Z. Xu and Y. Xia, Progress, Challenges and Perspectives of Computational Studies on Glassy Superionic Conductors for Solid-State Batteries, J. Mater. Chem. A 10, 11854 (2022).
- [4] S. Kalnaus, N. J. Dudney, A. S. Westover, E. Herbert, and S. Hackney, *Solid-State Batteries: The Critical Role of Mechanics*, Science **381**, eabg5998 (2023).
- [5] A. Sakuda, A. Hayashi, Y. Takigawa, K. Higashi, and M. Tatsumisago, Evaluation of Elastic Modulus of Li<sub>2</sub>S-P<sub>2</sub>S<sub>5</sub> Glassy Solid Electrolyte by Ultrasonic Sound Velocity Measurement and Compression Test, J. Ceram. Soc. Jpn. 121, 946 (2013).
- [6] A. Kato, M. Nose, M. Yamamoto, A. Sakuda, A. Hayashi, and M. Tatsumisago, *Mechanical Properties of Sulfide Glasses in All-Solid-State Batteries*, J. Ceram. Soc. Jpn. **126**, 719 (2018).
- [7] H. Eckert, Z. Zhang, and J. H. Kennedy, Structural Transformation of Non-Oxide Chalcogenide Glasses. The Short-Range Order of Lithium Sulfide (Li2S)-Phosphorus Pentasulfide (P2S5) Glasses Studied by Quantitative Phosphorus-31, Lithium-6, and Lithium-7 High-Resolution Solid-State NMR, Chem. Mater. 2, 273 (1990).
- [8] A. Hayashi, S. Hama, H. Morimoto, M. Tatsumisago, and T. Minami, Preparation of Li2S-P2S5 Amorphous Solid Electrolytes by Mechanical Milling, J. Am. Ceram. Soc. 84, 477 (2004).
- [9] A. Hayashi, Y. Ishikawa, S. Hama, T. Minami, and M. Tatsumisago, *Fast Lithium-Ion Conducting Glass-Ceramics in the System Li* <sub>2</sub> S SiS <sub>2</sub> P <sub>2</sub> S <sub>5</sub>, Electrochem. Solid-State Lett. **6**, A47 (2003).
- [10]H. Eckert, J. H. Kennedy, A. Pradel, and M. Ribes, Structural Transformation of Thiosilicate Glasses: 29Si MAS-NMR Evidence for Edge-Sharing in the System Li2S \(\subsetendet{B}iS2\), J. Non-Cryst. Solids 113, 287 (1989).
- [11]K. Mori, K. Iwase, Y. Oba, K. Ikeda, T. Otomo, and T. Fukunaga, *Structural and Electrochemical Features of (Li2S) (SiS2)100– Superionic Glasses*, Solid State Ion. **344**, 115141 (2020).
- [12]H. Morimoto, H. Yamashita, M. Tatsumisago, and T. Minami, Synthesis of the High Lithium Ion Conductive Amorphous in the Systems Li2S-SiS2 and Li2S-SiS2-Li4SiO4, J. Ceram. Soc. Jpn. (2000).
- [13] J. H. Kennedy and Z. Zhang, Preparation and Electrochemical Properties of the SiS2 P 2 S 5 Li2 S Glass Coformer System, J. Electrochem. Soc. 136, 2441 (1989).
- [14]R. Zhao, G. Hu, S. Kmiec, J. Wheaton, V. M. Torres, and S. W. Martin, *Grain-Boundary-Free Glassy Solid Electrolytes Based on Sulfide Materials: Effects of Oxygen and Nitrogen Doping on Electrochemical Performance*, Batter. Supercaps 5, (2022).
- [15]K. Ohara et al., Structural and Electronic Features of Binary Li2S-P2S5 Glasses, Sci. Rep. 6, 21302 (2016).

- [16]T. Ohkubo, K. Ohara, and E. Tsuchida, Conduction Mechanism in 70Li <sub>2</sub> S-30P <sub>2</sub> S <sub>5</sub> Glass by Ab Initio Molecular Dynamics Simulations: Comparison with Li <sub>7</sub> P <sub>3</sub> S <sub>11</sub> Crystal, ACS Appl. Mater. Interfaces 12, 25736 (2020).
- [17]M. Sadowski and K. Albe, Computational Study of Crystalline and Glassy Lithium Thiophosphates: Structure, Thermodynamic Stability and Transport Properties, J. Power Sources **478**, 229041 (2020).
- [18]X. He, Y. Zhu, A. Epstein, and Y. Mo, Statistical Variances of Diffusional Properties from Ab Initio Molecular Dynamics Simulations, Npj Comput. Mater. 4, 18 (2018).
- [19] S. Ariga, T. Ohkubo, S. Urata, Y. Imamura, and T. Taniguchi, *A New Universal Force-Field for the Li 2 S–P 2 S 5 System*, Phys. Chem. Chem. Phys. **24**, 2567 (2022).
- [20]L.-M. Poitras and M. Micoulaut, *Establishment of an Empirical Force-Field for Crystalline and Amorphous Li 2 S SiS 2 Electrolytes*, Phys. Rev. B **107**, 214205 (2023).
- [21]O. T. Unke, S. Chmiela, H. E. Sauceda, M. Gastegger, I. Poltavsky, K. T. Schütt, A. Tkatchenko, and K.-R. Müller, *Machine Learning Force Fields*, Chem. Rev. 45 (n.d.).
- [22]Z. Xu, H. Duan, Z. Dou, M. Zheng, Y. Lin, Y. Xia, H. Zhao, and Y. Xia, *Machine Learning Molecular Dynamics Simulation Identifying Weakly Negative Effect of Polyanion Rotation on Li-Ion Migration*, Npj Comput. Mater. **9**, 105 (2023).
- [23] J. Huang, L. Zhang, H. Wang, J. Zhao, J. Cheng, and W. E, *Deep Potential Generation Scheme and Simulation Protocol for the Li10GeP2S12-Type Superionic Conductors*, J. Chem. Phys. **154**, 094703 (2021).
- [24] G. Kresse and J. Hafner, Ab Initio *Molecular Dynamics for Liquid Metals*, Phys. Rev. B **47**, 558 (1993).
- [25]G. Kresse and J. Furthmüller, *Efficiency of Ab-Initio Total Energy Calculations for Metals and Semiconductors Using a Plane-Wave Basis Set*, Comput. Mater. Sci. **6**, 15 (1996).
- [26] G. Kresse and J. Furthmüller, *Efficient Iterative Schemes for* Ab Initio *Total-Energy Calculations Using a Plane-Wave Basis Set*, Phys. Rev. B **54**, 11169 (1996).
- [27] J. P. Perdew, A. Ruzsinszky, G. I. Csonka, O. A. Vydrov, G. E. Scuseria, L. A. Constantin, X. Zhou, and K. Burke, *Restoring the Density-Gradient Expansion for Exchange in Solids and Surfaces*, Phys. Rev. Lett. **100**, 136406 (2008).
- [28] H. Wang, L. Zhang, J. Han, and W. E, *DeePMD-Kit: A Deep Learning Package for Many-Body Potential Energy Representation and Molecular Dynamics*, Comput. Phys. Commun. **228**, 178 (2018).
- [29] Y. Zhang, H. Wang, W. Chen, J. Zeng, L. Zhang, H. Wang, and W. E, *DP-GEN: A Concurrent Learning Platform for the Generation of Reliable Deep Learning Based Potential Energy Models*, Comput. Phys. Commun. **253**, 107206 (2020).
- [30] A. Jain et al., Commentary: The Materials Project: A Materials Genome Approach to Accelerating Materials Innovation, APL Mater. 1, 011002 (2013).
- [31] L. Martínez, R. Andrade, E. G. Birgin, and J. M. Martínez, *PACKMOL: A Package for Building Initial Configurations for Molecular Dynamics Simulations*, J. Comput. Chem. **30**, 2157 (2009).
- [32] A. P. Thompson et al., *LAMMPS a Flexible Simulation Tool for Particle-Based Materials Modeling at the Atomic, Meso, and Continuum Scales*, Comput. Phys. Commun. **271**, 108171 (2022).
- [33] A. Stukowski, Visualization and Analysis of Atomistic Simulation Data with OVITO-the Open Visualization Tool, Model. Simul. Mater. Sci. Eng. 18, (2010).
- [34]G. Clavier, N. Desbiens, E. Bourasseau, V. Lachet, N. Brusselle-Dupend, and B. Rousseau, Computation of Elastic Constants of Solids Using Molecular Simulation: Comparison of Constant Volume and Constant Pressure Ensemble Methods, Mol. Simul. 43, 1413 (2017).
- [35] A. P. Thompson, S. J. Plimpton, and W. Mattson, *General Formulation of Pressure and Stress Tensor for Arbitrary Many-Body Interaction Potentials under Periodic Boundary Conditions*, J. Chem. Phys. **131**, 154107 (2009).
- [36] R. Gaillac, P. Pullumbi, and F.-X. Coudert, *ELATE: An Open-Source Online Application for Analysis and Visualization of Elastic Tensors*, J. Phys. Condens. Matter **28**, 275201 (2016).

- [37] A. Pradel and A. Piarristeguy, *Thio and Selenosilicates, Sulfide and Selenide Counterparts of Silicates: Similarities and Differences*, Comptes Rendus Géoscience **354**, 79 (2022).
- [38] J. M. Whiteley, J. H. Woo, E. Hu, K.-W. Nam, and S.-H. Lee, *Empowering the Lithium Metal Battery through a Silicon-Based Superionic Conductor*, J. Electrochem. Soc. **161**, A1812 (2014).
- [39]P. Bron, S. Johansson, K. Zick, J. Schmedt Auf Der Günne, S. Dehnen, and B. Roling, *Li* <sub>10</sub> *SnP* <sub>2</sub> *S* <sub>12</sub> : *An Affordable Lithium Superionic Conductor*, J. Am. Chem. Soc. **135**, 15694 (2013).
- [40] J. G. Smith and D. J. Siegel, *Low-Temperature Paddlewheel Effect in Glassy Solid Electrolytes*, Nat. Commun. 11, 1483 (2020).
- [41] A. Kato, M. Yamamoto, A. Sakuda, A. Hayashi, and M. Tatsumisago, *Mechanical Properties of Li* <sup>2</sup> S–P <sup>2</sup> S <sup>5</sup> Glasses with Lithium Halides and Application in All-Solid-State Batteries, ACS Appl. Energy Mater. 1, 1002 (2018).
- [42]T. Baba and Y. Kawamura, Structure and Ionic Conductivity of Li2S–P2S5 Glass Electrolytes Simulated with First-Principles Molecular Dynamics, Front. Energy Res. 4, (2016).
- [43] Z. Deng, Z. Wang, I.-H. Chu, J. Luo, and S. P. Ong, *Elastic Properties of Alkali Superionic Conductor Electrolytes from First Principles Calculations*, J. Electrochem. Soc. **163**, A67 (2016).
- [44] L. Deng and J. Du, Effects of System Size and Cooling Rate on the Structure and Properties of Sodium Borosilicate Glasses from Molecular Dynamics Simulations, J. Chem. Phys. **148**, 024504 (2018).
- [45] A. Pradel and M. Ribes, *Electrical Properties of Lithium Conductive Silicon Sulfide Glasses Prepared by Twin Roller Quenching*, Solid State Ion. **18–19**, 351 (1986).
- [46] S. Ohno et al., How Certain Are the Reported Ionic Conductivities of Thiophosphate-Based Solid Electrolytes? An Interlaboratory Study, ACS Energy Lett. 5, 910 (2020).
- [47]Ö. U. Kudu et al., Structural Details in Li3PS4: Variety in Thiophosphate Building Blocks and Correlation to Ion Transport, Energy Storage Mater. 44, 168 (2022).
- [48] M. Tatsumisago, F. Mizuno, and A. Hayashi, *All-Solid-State Lithium Secondary Batteries Using Sulfide-Based Glass-Ceramic Electrolytes*, J. Power Sources **159**, 193 (2006).
- [49]Z. Zhang and H. Kennedy, SYNTHESIS AND CHARACTERIZATION OF THE B2S3-Li2S, THE P2S5-Li2S AND THE B2S3-P2S5-Li2S GLASS SYSTEMS, (n.d.).
- [50] J. H. Kennedy and Z. Zhang, *Improved Stability for the SiS2-P2S5-Li2S-Li1 Glass System*, Solid State Ion. **28–30**, 726 (1988).
- [51] W. Kabsch, A Solution for the Best Rotation to Relate Two Sets of Vectors, Acta Crystallogr. Sect. A 32, 922 (1976).
- [52] Z. Zhang, H. Li, K. Kaup, L. Zhou, P.-N. Roy, and L. F. Nazar, *Targeting Superionic Conductivity by Turning on Anion Rotation at Room Temperature in Fast Ion Conductors*, Matter **2**, 1667 (2020).

**TOC Figure** 

# Machine Learning Force Field



# **Supplementary Information for**

A Machine Learning Force Field for Lithium Sulfide Glassy Electrolytes and its Comprehensive Validation and Application

Rui Zhou, Kun Luo, Steve W. Martin, and Qi An\*

Department of Materials Science and Engineering, Iowa State University, Ames, Iowa 50011, United States

Corresponding Author's email: qan@iastate.edu

Table S1. Detailed local environment of P in 60Li2S-32SiS2-8P2S5 glass from ML-FF

# of Bridging sulfur (Q <sup>n</sup> )	# of Edge-sharing units (E <sup>n</sup> )	P-S-X	P-X	Population
0	0			60.78%
0	0		P	8.98%
1	0	Si		16.80%
1	0	Si	P	1.02%
1	0	P		3.44%
2	0	Si, Si		1.17%
2	0	Si, Si	P	0.16%
2	0	Si, P		1.80%
2	0	P, P		0.08%
2	1	Si, Si		5.00%
2	1	P, P		0.16%
2	1	Si, Si	P	0.08%
3	0	Si, Si, Si		0.08%
3	1	Si, Si, Si		0.31%
3	1	Si, Si, P		0.16%

Table S2. Detailed local environment of Si in 60Li2S-32SiS2-8P2S5 glass from ML-FF

# of Bridging sulfur	# of Edge- sharing units	Si-S-X	Population
0	0		20.23%
1	0	Si	21.72%
1	0	P, P	3.59%
2	0	Si, Si	7.89%
2	0	Si, P	3.24%
2	0	P, P	0.82%
2	1	Si, Si	29.45%
2	1	P, P	2.77%
3	0	Si, Si, Si	0.70%
3	0	Si, Si, P	0.20%
3	1	Si, Si, Si	6.37%
3	1	Si, Si, P	1.95%
3	1	Si, P, P	0.51%
3	1	P, P, P	0.08%
4	1	Si, Si, Si, Si	0.12%
4	1	Si, P, P, P	0.04%
4	2	Si, Si, Si, Si	0.31%